HHS Public Access

Author manuscript

Nano Lett. Author manuscript; available in PMC 2021 September 09.

Published in final edited form as:

Nano Lett. 2020 September 09; 20(9): 6510–6519. doi:10.1021/acs.nanolett.0c02248.

Prevention of Hepatic Ischemia-Reperfusion Injury by Carbohydrate-Derived Nanoantioxidants

Yin Long[#],
Department of Material Science and Engineering, University of Wisconsin - Madison, Madison, Wisconsin 53706, United States

Hao Wei[#],
Departments of Radiology and Medical Physics, University of Wisconsin - Madison, Madison, Wisconsin 53705, United States; Department of Nuclear Medicine, Union Hospital, Tongji Medical College, Huazhong University of Science and Technology, Wuhan 430073, China; University of Wisconsin Carbone Cancer Center, Madison, Wisconsin 53705, United States

Jun Li,
Department of Material Science and Engineering, University of Wisconsin - Madison, Madison, Wisconsin 53706, United States

Mengting Li,
Departments of Radiology and Medical Physics, University of Wisconsin - Madison, Madison, Wisconsin 53705, United States; Department of Nuclear Medicine, Union Hospital, Tongji Medical College, Huazhong University of Science and Technology, Wuhan 430073, China; University of Wisconsin Carbone Cancer Center, Madison, Wisconsin 53705, United States

Yizhan Wang,
Department of Material Science and Engineering, University of Wisconsin - Madison, Madison, Wisconsin 53706, United States

Ziyi Zhang,

Corresponding Authors: Hao Wei – Departments of Radiology and Medical Physics, University of Wisconsin - Madison, Madison, Wisconsin 53705, United States; Department of Nuclear Medicine, Union Hospital, Tongji Medical College, Huazhong University of Science and Technology, Wuhan 430073, China; University of Wisconsin Carbone Cancer Center, Madison, Wisconsin 53705, United States; hwei52@wisc.edu, Weibo Cai – Departments of Radiology and Medical Physics, University of Wisconsin - Madison, Madison, Wisconsin 53705, United States; University of Wisconsin Carbone Cancer Center, Madison, Wisconsin 53705, United States; wcai@uwhealthy.org, Xudong Wang – Department of Material Science and Engineering, University of Wisconsin - Madison, Madison, Wisconsin 53706, United States; xudong.wang@wisc.edu.

[#]Y.L. and H.W. contributed equally to this work.

Author Contributions

Y.L., H.W., X.D.W., and W.B.C. conceived the idea and designed the study. H.W. and Y.L. conducted the experiments with assistance from J.L., M.T.L., and Z.Y.Z. Y.Z.W. performed the TEM, C.C. performed the AFM. T.Y.C., T.W.S., and D.W.J. helped with the PET imaging. X.L.L. and Y.D.J. contributed to the discussion and provided advice. J.W.E. produced Zr-89. X.D.W. and W.B.C. supervised the whole research. All of the authors participated in the preparation of the manuscript.

Complete contact information is available at: https://pubs.acs.org/10.1021/acs.nanolett.0c02248

Supporting Information

The Supporting Information is available free of charge at https://pubs.acs.org/doi/10.1021/acs.nanolett.0c02248.
Experimental details; AFM images, XPS spectra, and UV–vis absorbance of C-NPs; optical image, XPS spectra and SEM characterizations of C-NP reaction with H_2O_2; in vitro cell viabilities and time-dependent cellular uptake of C-NPs; autoradiography of TLC plates; 89Zr labeling yields PET images of mice i.v. injected with ^{89}Zr–C–NPs and free Zr-89; cytotoxicity evaluation on liver; long-term cytotoxicity on blood serum; H&E-stained images from major organs; Suzuki Score of liver (PDF)

The authors declare no competing financial interest.

Department of Material Science and Engineering, University of Wisconsin - Madison, Madison, Wisconsin 53706, United States

Tianye Cao,
Departments of Radiology and Medical Physics, University of Wisconsin - Madison, Madison, Wisconsin 53705, United States; University of Wisconsin Carbone Cancer Center, Madison, Wisconsin 53705, United States

Corey Carlos,
Department of Material Science and Engineering, University of Wisconsin - Madison, Madison, Wisconsin 53706, United States

Lazarus G. German,
Department of Material Science and Engineering, University of Wisconsin - Madison, Madison, Wisconsin 53706, United States

Dawei Jiang,
Departments of Radiology and Medical Physics, University of Wisconsin - Madison, Madison, Wisconsin 53705, United States; University of Wisconsin Carbone Cancer Center, Madison, Wisconsin 53705, United States

Tuanwei Sun,
Departments of Radiology and Medical Physics, University of Wisconsin - Madison, Madison, Wisconsin 53705, United States; University of Wisconsin Carbone Cancer Center, Madison, Wisconsin 53705, United States

Jonathan W. Engle,
Departments of Radiology and Medical Physics, University of Wisconsin - Madison, Madison, Wisconsin 53705, United States

Xiaoli Lan,
Department of Nuclear Medicine, Union Hospital, Tongji Medical College, Huazhong University of Science and Technology, Wuhan 430073, China

Yadong Jiang,
State Key Laboratory of Thin Films and Integrated Devices, School of Optical Science and Engineering, University of Electronic Science and Technology of China, Chengdu 610054, China

Weibo Cai,
Departments of Radiology and Medical Physics, University of Wisconsin - Madison, Madison, Wisconsin 53705, United States; University of Wisconsin Carbone Cancer Center, Madison, Wisconsin 53705, United States

Xudong Wang
Department of Material Science and Engineering, University of Wisconsin - Madison, Madison, Wisconsin 53706, United States

Abstract

Hepatic ischemia-reperfusion injury (IRI), which mainly results from excessive reactive oxygen species (ROS) generated by a reperfusion burst of oxygen, has long been a major cause of liver

dysfunction and failure after surgical procedures. Here, a monodispersed hydrophilic carbohydrate-derived nanoparticle (C-NP) was synthesized as a nanoantioxidant that could effectively prevent hepatic IRI. The spherical C-NPs had a size of ~78 ± 11.3 nm covered with polar surface groups. They were well dispersible in water with good colloidal stability, nontoxicity, and good ROS scavenging capability. The C-NPs also exhibited good circulation lifetime, effective delivery to liver, and gradual degradability with an ability to assist the IRI group maintaining a normal and healthy liver status. The pathology mechanism of C-NPs in hepatic IRI was confirmed to be scavenging of excessive ROS by C-NPs. The effective therapeutic treatment of C-NPs in living animals revealed a great potential in clinical prevention for hepatic IRI.

Graphical Abstract

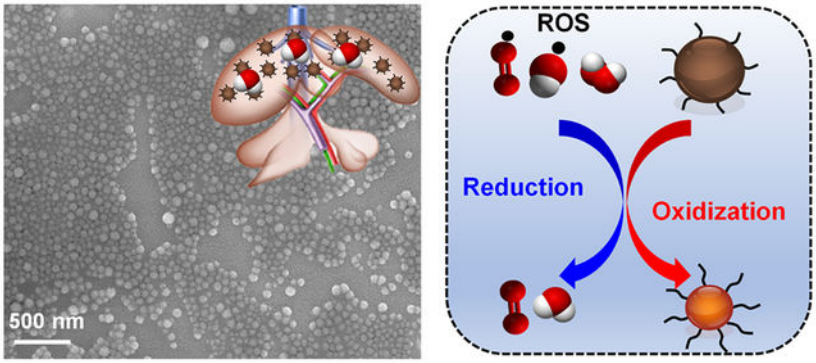

Keywords

Carbohydrate-derived nanoparticles; Ischemia-reperfusion injury; Reactive oxygen species scavenging; Nanoantioxidant; Colloidal

INTRODUCTION

Organ ischemia with inadequate oxygen supply followed by reperfusion can lead to complex inflammatory responses and oxidative stress. Liver is highly dependent on oxygen supply and susceptible to hypoxic or anoxic conditions.[1] Hepatic ischemia-reperfusion injury (IRI) is therefore a major cause of liver dysfunction and failure after surgical procedures such as tissue resection, trauma, hypovolemic shock, and transplantation.[2,3] Reactive oxygen species (ROS), such as hydrogen peroxide (H_2O_2), superoxide anion (O^{2-}), and hydroxyl radical (HO^-), play a major role in reperfusion injury by peroxidation of DNA, protein, and lipids, which can cause a series of deleterious cellular responses including cell death, inflammation, and ultimate hepatic failure.[4–6] It is, therefore, essential to develop methodologies capable of eliminating ROS during reperfusion to prevent and treat hepatic IRI.[7,8] However, there is no approved clinical pharmacological intervention for hepatic IRI.[9] Recently, various nanomaterials have been developed with ROS scavenging ability to treat ROS-related diseases including stroke,[10] neurodegenerative diseases,[11] acute kidney injury,[12] atherosclerosis,[13] and diabetes.[14] These nanomaterials are mostly made from metal and metal oxides, such as platinum,[15] gold[16] and selenium[17] and ceria oxides.[18,19] However, these nanomaterials face several critical hurdles for clinical translation, that is, easy to

aggregate (poor colloidal stability)[20] in the bloodstream or in the liver/spleen system, metal-ion release side effects,[21] poor degradability,[22] and the requirement of extra surface coating/functionalization to achieve desired biodistribution and biostability may jeopardize the reaction kinetics of ROS.

Specifically, carbon-based nanomaterials such as carboxyl-modified fullerenes with a conjugated π-system have already shown excellent capability of ROS harvesting related applications.[22–24] Herein, unlike common hydrophobic carbon materials, a hydrophilic carbohydrate-derived nanoparticle (C-NP) was synthesized by a one-step aqueous method[25] and directly applied as an effective nanoantioxidant for the first time. This C-NP contains polyfurane units with conjugated π-systems of which antioxidant chemistry is based on radical capture and reaction on conjugated π-systems and unsaturated bonds.[26,27] The hydrophilicity due to polar surface groups enables excellent dispensability in water with good colloidal stability. *In vitro* cytotoxicity and ROS scavenging experiments demonstrated a great potential in preventing ROS-related diseases. Therefore, these C-NPs were further applied *in vivo* and successfully ameliorated acute liver injury in hepatic IRI models. Two clinical liver damage indicators (the aspartate aminotransferase (AST) and alanine aminotransferase (ALT) levels) showed that a C-NP-treated group had negligible liver damage and it enhanced recovering the superoxide dismutase (SOD) level to the normal healthy state within 60 h. The detailed mechanism of IRI prevention by C-NPs was investigated systematically, including roles of liver sinusoidal endothelial cells, Kupffer cells, and monocyte/macrophage cells, the release of pro-inflammatory cytokines, and the recruitment and infiltration of neutrophils. This study provided a novel strategy for effectively treating hepatic IRI.

RESULTS AND DISCUSSION

Physiochemical Properties of C-NPs.

Scanning electron microscopy (SEM) and transmission electron microscopy (TEM) images shown in Figure 1a revealed that as-received C-NPs had a uniform spherical shape with a monodispersed size distribution.[28] The phase of the products was confirmed by X-ray diffraction (XRD) spectra. The broad peak centered at about 25.3° corresponds to the amorphous structure of the polymer-like carbons. The (101) peak (about 42°) relates to in-plane scattering and is characteristic of a turbostratic-type (sp^2-hybridized) carbon due to aromatization and condensation of the materials.[29,30] The as-prepared C-NPs could be easily dispersed (Zeta potential: −68.1 ± 0.37 mV) in an aqueous solution (Figure 1b) and maintain colloidal stability in PBS solution for at least 3 days. Size distribution of the C-NPs was measured by dynamic light scattering (DLS) analysis and showed an average diameter of 78 ± 11.3 nm (Figure 1c). The C-NPs exhibited a relatively uniform spherical morphology at a larger scale, as confirmed by the repeatable wavy height profile from atomic force microscopy (AFM) (Figure S1) scan. The surface of sphere was generally smooth with no obvious roughness.

X-ray photoelectron spectroscopy (XPS) analysis was performed to investigate the composition of the C-NPs. The full spectrum survey showed two major components, C (62.23%) and O (30.39%) from the C-NPs (Figure S2). The enlarged C 1s peak (Figure 1d)

could be deconvoluted into three main components including C—C, C—O, and C=O. Accordingly, the O 1s peak (Figure 1e) could also be deconvoluted to two oxygen bonds, that is, C—O and C=O. Fourier-transform infrared (FTIR) spectroscopy (Figure 1f) further showed the vibration bands from C=O groups at 1710 cm^{-1} and aromatic C=C groups at 1620 and 1513 cm^{-1}. Bands in the range of 1000–1300 cm^{-1}, corresponding to the C–OH stretching and OH bending vibrations, implied the existence of residual hydroxyl groups. The hydroxyl groups could be covalently bonded to the carbonized core and contributed to the hydrophilicity and stability of C-NPs. Comparing the C-NPs to the precursor (glucose) showed that the aromatic C—H bands at 875–750 cm^{-1} disappeared, whereas aliphatic C=C and C—O—H (hydroxyl or carboxyl) bands appeared at ~2900 and 3000–3700 cm^{-1}, respectively, indicating the occurrence of dehydration and aromatization during the hydrothermal carbonization, which were responsible for generating turbostratic-type carbon structure.

In Vitro ROS Scavenging by C-NPs.

The ROS scavenging capability of the C-NPs was first investigated *in vitro* in a cell-free system by in situ Raman, electrospin resonance (ESR) and UV–vis absorbance spectroscopy. The Raman spectra of the pristine C-NPs (Figure 2a) showed two overlapping bands around 1589 and 1361 cm^{-1} which could be attributed to the in-plane vibrations in aromatic crystalline carbon (G band)[31] and disordered amorphous (partially hydrogenated) carbon films (D band),[32] respectively. These data confirmed the existence of small aromatic clusters in C-NP samples, agreeing well with the aromatization of the materials observed in FTIR spectra. After adding H_2O_2, a strong new peak centered at 875 cm^{-1} appeared corresponding to H_2O_2, while both D and G bands of C-NPs were almost flattened out. After 30 min, the H_2O_2 peak decreased and peaks of C-NPs were re-emerging. Finally, the H_2O_2 peak fully disappeared and a new CO_3^{2-} peak emerged as a result of oxidation of carbohydrate and formation of dissolvable carbonates. The significantly stronger G band compared to D band post reaction suggested that amorphous carbon was more reactive and receptive to H_2O_2. The strong antioxidative ability was also shown by ESR spectra (Figure 2b), where the 1:2:2:1 multiple peaks represent the •OH captured by 5,5′-dimethylpyrroline-1-oxide (DMPO) as a spin trapping agent. The peak intensity was highly sensitive to the amount of trapped DMPO/•OH, which was dependent on the scavenging ability of C-NPs. The peaks showed a sharp decrease upon adding C-NPs and further decreased as the C-NP concentration increased, revealing that the remaining ROS was highly responsive to the C-NP concentration. Moreover, pristine C-NPs exhibited a maximum absorption peak at ~240 nm (Figure 2c), which linearly decreased (Figure S3) as the amount of H_2O_2 increased. This correlation can also be clearly observed from the color degradation of 5 μg/mL C-NPs solution when adding 0–450 μM of H_2O_2 (Figure S4). SEM analysis of the degrading samples was shown in Figure S5; after adding over 250 μM H_2O_2, the C-NPs transformed to dissolvable carbonates (increased dendrite clusters appears), which was in consistent with former results in Raman spectra (the CO_3^{2-} peak emerged). More XPS analyses (Figure S6) of C-NPs reacting with H_2O_2 demonstrated an increased O/C ratio in the products of C-NP/H_2O_2 system (Figure S7), confirming the oxidation of unsaturated C=C with H_2O_2 and generation of dissolvable carbonates. *In vitro* antioxidative experiments further conducted on comprehensive ROS assays were using catalase (CAT), hydroxyl radical antioxidant

capacity (HORAC), and superoxide dismutase (SOD) activity bioassays to evaluate H_2O_2, •OH, and O_2^-, respectively. The results shown in Figure 2d–f demonstrated that the activities of all anti-ROS enzymes were highly dependent on the concentration of C-NPs, further confirming the *in vitro* effectiveness of C-NPs as an antioxidant.

A time- and dose-dependent viability assay was then employed to evaluate the cellular effects/cytotoxicity of the C-NPs. The embryonic kidney 293 (HEK293) cell viability test (shown in Figure S8) confirmed that the as-prepared C-NPs had no significant toxicity. The cellular uptake of C-NPs by RAW264.7 cells increased along with the incubate time increased from 0 to 24 h (Figure S9), demonstrating the capability of C-NPs entering cells and harvesting ROS *in situ*. ROS scavenging ability of C-NPs in HepG2 (human hepatocellular carcinoma) cell system was investigated by comparing the immunofluorescent confocal images shown in Figure 2g, where ROS and nuclei were stained as green and blue, respectively. Normal ROS signals (green signal) generated by cell breathing could be found in the cell system with added PBS and C-NPs solutions (left two images in the top row). Much stronger and intensive ROS signals could be clearly seen in H_2O_2-containing cell systems (two middle images in the top row). Accordingly, massive cell death occurred as confirmed by membrane damage/disappearing and nuclei leaking out/merging in Hoechst staining images (middle row). With the presence of C-NPs (right column), the ROS signal was significantly suppressed nearly to the level of the two control systems and the cell death was dramatically reduced. To quantify the relationship of cell viability with the C-NPs concentration, *in vitro* cell viability test of human embryonic kidney (HEK293) cells with 250 μM H_2O_2 and C-NPs ranging from 5–25 μg/mL were compared (Figure 2h). It could be clearly seen that the survival rate of HEK293 cells were highly dependent on the concentration of C-NPs. In general, the *in vitro* experiments suggested that the C-NPs were nontoxic and could effectively scavenge ROS and thus protect the cells from ROS damage.

In Vivo Biophysiochemical Study of C-NPs.

In vivo PET imaging was used to investigate the biodistribution of C-NPs. The radionuclide ^{89}Zr was used to label C-NPs,[33] and the resultant ^{89}Zr–C–NPs were highly stable in PBS solution as monitored by thin layer chromatography (Figure S10). The labeling yield increased following the time and temperature and reached 69% at 15 °C and 89.1% at 55 °C after 2.5 h incubation (Figure S11). Real-time and noninvasive trace of ^{89}Zr–C–NPs were recorded by PET imaging after mice received intravenous (i.v.) injection of 89Zr–C–NPs. As shown in Figures 3a and S12, the maximum intensity projection (MIP) images displayed a clear vision of the heat signal at 12 h post injection (p.i.), indicating a good circulation of the NPs. A dramatic signal increase also presented in the bladder after 1 h, which could be a sign of renal clearance of the excessive injected nanoparticles since no signal of bone and joint absorption of free Zr-89 was observed at this time point (Figure S12). This observation was intriguing as excessive NPs were able to be efficiently excreted via urine, an ideal property of nanomedicine that should home efficiently to the desired/diseased area with the unbounded quickly excreted by renal clearance, avoiding extended duration in the host. Such an ideal circulation capability could be attributed to the unique carboxyl group-decorated amorphous carbon structure. The carboxyl coating created a hydrophilic protection layer

around the C-NPs, which could repel the absorption of opsonin proteins via steric repulsion, and thereby significantly delayed the first step in opsonization.[34] Therefore, the C-NPs could maintain good colloidal stability in blood circulation and meanwhile still possess a strong capacity to pass across microcapillaries.

Signals in the liver and spleen were found at 1 h p.i. and became exclusive at 24 h p.i. After 48 h p.i., ^{89}Zr–C–NPs started to degrade gradually, showing a major signal in the vertebra (Figure S12), since free ^{89}Zr could easily be absorbed by bones and joints (Figure S13).[35] Quantitative region-of interest (ROI) analysis of PET images in Figure 3b showed that the liver uptake of ^{89}Zr–C–NPs peaked at 24 h p.i (25.6 ± 1.7%/ID/g) followed by subsequent decrease to the original level. This observation suggested that the NPs were gradually cleared from the liver starting from day 1.

Prevention of Hepatic IRI in Murine Model.

A murine model of IRI was created according to a previous protocol.[36] The treatment effect of C-NPs to hepatic IRI was tested by i.v. injecting C-NPs to IRI-mice, which was compared to two control groups, including an IRI group with PBS injection (Figure 4a) and a sham-operated group that exposed liver but without ligation. The blood/liver samples were collected from all groups and analyzed to evaluate the liver function at 12 h after surgery. Another group of C-NP-treated IRI mice was examined at 60 h after the surgery for long-term assessment. Hematoxylin and eosin (H&E) staining of liver tissues was performed to provide direct evidence of IRI treatment. Large areas of severe damage were found (white dashed line area in Figure 4b) in liver sections from PBS-treated IRI mice along with obvious cytolysis, necrosis of hepatic cells, and hemorrhage. Such a massive necrosis was also found in the PBS-treated IRI group after 60 h, which indicated the damage already overrids the liver self-healing ability. However, from the 12 h C-NPs-treated IRI group, only slight cell vacuolization (yellow arrow) generated by osmosis was discovered. No obvious damage could be observed in the C-NP-treated IRI group after 60 h. Their H&E staining results were similar to those of healthy mice received PBS (sham group, first picture in the top row in Figure 4b) or C-NP injection (first picture in the bottom row in Figure 4b). Sections were scored from 0 to 4 for sinusoidal congestion, vacuolization of hepatocyte cytoplasm, and parenchymal necrosis, as described by Suzuki et al.[37] (Tables S1 and S2), and the C-NP-treated IRI group had a 71.42% lower value compared to the PBS-treated IRI group, further confirming that the C-NPs can successfully prevent IRI damage in liver (Tables S1 and S2).

In clinical study for hepatic injury, aspartate aminotransferase (AST) and alanine aminotransferase (ALT) levels are key and universal indicators for liver health raging from early preclinical animal testing to postmarketing patient monitoring.[38,39] The AST and ALT levels were significantly elevated in the IRI mice group, indicating severe liver damage. In contrast, these two indicators were very low in the C-NPs injected group and sham group, evidencing the successful prevention of liver damage by C-NPs *in vivo*. Furthermore, the superoxide dismutase (SOD) level was tested in liver homogenates from all groups. SOD is a main self-defender to neutralize ROS from nearby cells in the liver, which is usually considered as an indicator of oxidative stress.[40] The PBS-treated IRI mice groups showed a

significantly reduced level of SOD due to the oxidative stress, while the C-NP-treated IRI group could maintain a normal SOD level as compared to the sham group and C-NP control group. All of these results together provided a convincing case that hepatic injury did occur in C-NP-treated IRI mouse, and C-NP injection can effectively prevent the injury. It is worthy to note that all of the ALT, AST, and SOD levels and H&E staining results from healthy mice injected with C-NPs were all in the normal range, demonstrating there was no toxic side effect of the C-NPs *in vivo*. The liver profile detection (Figures S14 and 15) (including cholesterol, albumin, urea nitrogen, and alkaline phosphatase) and H&E staining of main organs (Figure S16) of mice that received C-NP treatment at both day 1 and day 15 confirmed the biocompatibility of C-NPs *in vivo*.

Pathophysiology of Hepatic IRI Prevention.

Activation of Kupffer Cells and Other Monocytes/Macrophages.—As excessive ROS is believed to regulate cellular phenotypes in liver during reperfusion, the generation and scavenging of ROS is the key mechanism of hepatice IRI injury/prevention.[41] Here we performed immunofluorenscene staining on liver samples to demonstrate the effect of cellular phenotypes. DAPI, Anti-CLE4F, anti-F4/80, and anti-CD31 antibodies were used for marking nuclear (blue), Kupffer cells (green), monocyte/macrophage cells (pink), and vascular endothelial cells (red), respectively. As shown in Figure 5a, both healthy mice treated with C-NPs and the sham group exhibited minimal monocyte/macrophage activation and intact vascular endothelial integrity. In contrast, hepatic IRI led to significant activation of monocytes/macrophages as well as impaired endothelial integrity. Moreover, Kuffper cells were obviously activated to accumulate around the damaged area, and the monocyte/macrophage cells migrated and gathered inside the area. At the same time, hepatocyte nuclei became pyknotic and karorrhexis 12 h after injury, then underwent karyolysis 60 h later. With C-NP scavenging excessive ROS, minimal aciviation of Kupffer cells and recruitment of monocyte/macrophages were found in liver staining slices. Activated Kupffer cells are responsible for releasing signals including pro-inflammatory cytokines, prostanoides, and ROS,[42] which activate more Kupffer cells and other immune cells and thus lead to more liver damage in the continued circle. To further confirm the cytoactivity of Kupffer cells and monocytes/macrophages, several cytokines in liver homogenates from each group were tested using enzyme-linked immunosorbent assay (ELISA). As shown in Figure 5b, a pro-inflammatory cytokine, interleukin-1 (IL-1), was significantly increased in the hepatic IRI groups, which were secreted by the first respondor macrophages exhibiting the inflammatory phenotype.[43] The IL-1 was reported to stimulate ROS release in neutrophils and would further increase tumor necrosis factor-α (TNF-α) (shown in Figure 5c synthesis in Kupffer cells). TNF-α is also a pro-inflammatory cytokine, which in turn promotes activation of Kupffer cells and monocytes/macrophages.[44] As a stimulator for innate immunity response, interleukin-6 (IL-6) was found to be up-regulated by TNF-α, which was shown in Figure 5d. Another pro-inflammatory cytokine, nitric oxide synthase 2 (NOS2), which is responsible for for high levels of NO,[45] was also up-regulated in the liver homogenates of nontreated IRI mice (Figure S17), thus highly toxic peroxynitrite anion was produced by the high level of NO combined with high oxidative stress. However, the NOS2 level was ameliorated in mice receiving C-NP treatment due to ROS scavenged by C-NPs effectively. In general, these pro-inflammatory cytokines, including IL-1, IL-6, TNF-α, and NOS2, were significantly

increased in the hepatic IRI groups while being maintained in normal ranges in C-NP-treated IRI mice. These upgraded cytokines further amplified activation of Kupffer cells, promoted neutrophil recruitment, and adherenced to the liver sinusoids, which were thoroughly investigated next.

Recruitment and Infiltration of Neutrophils.—The interferon gamma (IFN-γ) and interleukin-12 (IL-12) secreted by activated Kupffer will further drive inflammatory response forward by recruitng the neutrophils to the inflammatory site within minutes[46,47] which is another key cellular phenotype during acute oxidative injury. The increased secretation of IFN- γ and IL-12 in the IRI group without protection of C-NPs was confirmed in Figure S19a,b, respectively. These two cytokines are reponsible for promoting the recuitment of neutrophils and apotosis of the hepacytes that were thoroughly evaluated by immunofluorescence staining on liver slices. Anti-intracellular adhesion molecule-1 (anti-ICAM-1) antibody was used as a marker for the adhesion of neutrophils and other immune cells. As shown in Figure S18, low ICAM-1 expression was found in healthy mice liver tissues treated with PBS or C-NPs and the sham group, together with intact endothelial integrity and negligible hepatocytes apoptosis. However, hepatic IRI showed very high expression of ICAM-1, hepatocytes apoptosis, and impaired endothelial integrity. For the C-NP-protected IRI group, all of these symptoms were reversely ameroliated at 12 and 60 h after treatment. High expression of the ICAM-1 on the intraluminal side of liver sinusoidal endothelial cells is believed to be responsible for the rolling, binding, and parenchymal extravasation of neutrophils.[48] Moreover, the infiltration of neutrophils was also immunostained and compared by using anti-Ly6G antibody as the neutrophil marker (shown in Figure S19c). High expression of neutrophil infiltration was found in liver tissues from IRI mice while mice receiving PBS and C-NPs-protected IRI mice exhibited minimal neutrophil infiltration in the liver tissue at both 12 and 60 h time point. Myeloperoxidase (MPO), as a heme-containing peroxidase mainly expressed in neutrophils, underwent an obvious growth in livers from hepatic IRI mice (Figure S19d). However, in the liver of C-NP-treated IRI mice, MPO was not much different to those of healthy mice both at 12 and 60 h time points, confirming less adhesion and infiltration of neutrophils in C-NP-protected liver tissues.

CONCLUSION

In summary, green-synthesized C-NPs were utilized as a nanoantioxidant for prevention of hepatic IRI. Physiochemical properties were characterized first to show good colloid stability and hydrophilicity inherited from carbohydrate precursors. The C-NPs contains polyfurane units with conjugated π-systems of which antioxidant chemistry is based on radical capture and reaction on conjugated π-systems and unsaturated bonds. Efficient ROS scavenging of these C-NPs was confirmed in different *in vitro* assays. *In vivo* PET imaging further demonstrated good degradability, good circulation ability, and accurate liver delivery of the C-NPs. *In vivo* hepatic IRI study in a murine animal model revealed that the C-NPs could effectively prevent the hepatic IRI and achieve normal liver function and restore SOD levels. This intriguing therapeutic effect was attributed to the strong capability of C-NPs in rapidly scavenging excessive ROS and thus suppressed the acitivation of Kupffer cells and

monocyte/macrophage cells, preventing them from releasing pro-inflammatory cytokines, subsequently minimizing the adhension, recruitment, and infiltration of neutrophils, and eventually inhibiting the continued inflammatory process.[46] This study provides a comprehensive study on the ROS scavenging by C-NPs for effective hepatic IRI prevention. It offers a promising potential solution for treating ROS-related diseases, such as Alzheimer's disease, Parkinson's disease, and stroke using carbon-based nanomaterials.

Supplementary Material

Refer to Web version on PubMed Central for supplementary material.

ACKNOWLEDGMENTS

This work was supported in part by the National Institutes of Health under Award Numbers R21EB027857 and P30 CA014520 and the National Natural Science Foundation of China (51373128).

REFERENCES

(1). Andrew TL; Swager TM A fluorescence turn-on mechanism to detect high explosives RDX and PETN. J. Am. Chem. Soc 2007, 129, 7254–7255. [PubMed: 17508754]

(2). Eltzschig HK; Eckle T Ischemia and reperfusion–from mechanism to translation. Nat. Med 2011, 17, 1391–401. [PubMed: 22064429]

(3). Monga SP Lipid metabolic reprogramming in hepatic ischemia-reperfusion injury. Nat. Med 2018, 24, 6–7. [PubMed: 29315298]

(4). Alban FT; Gyamfi D; van Golen RF; Heger M Reactive Oxygen and Nitrogen Species and Liver Ischemia-Reperfusion Injury: An Overview In The Liver; Elsevier, 2018; pp 79–96.

(5). Bhogal RH; Weston CJ; Velduis S; Leuvenink HGD; Reynolds GM; Davies S; Nyguet-Thin L; Alfaifi M; Shepard EL; Boteon Y; Wallace L; Oo YH; Adams DH; Mirza DF; Mergental H; Muirhead G; Stephenson BTF; Afford SC The Reactive Oxygen Species-Mitophagy Signaling Pathway Regulates Liver Endothelial Cell Survival During Ischemia/Reperfusion Injury. Liver Transpl. 2018, 24, 1437–1452. [PubMed: 30040176]

(6). Fondevila C; Busuttil RW; Kupiec-Weglinski JW Hepatic ischemia/reperfusion injury—a fresh look. Exp. Mol. Pathol 2003, 74, 86–93. [PubMed: 12710939]

(7). He SQ; Zhang YH; Venugopal SK; Dicus CW; Perez RV; Ramsamooj R; Nantz MH; Zern MA; Wu J Delivery of antioxidative enzyme genes protects against ischemia/reperfusion-induced liver injury in mice. Liver Transpl. 2006, 12, 1869–79. [PubMed: 17133584]

(8). Chouchani ET; Pell VR; Gaude E; Aksentijevic D; Sundier SY; Robb EL; Logan A; Nadtochiy SM; Ord ENJ; Smith AC; Eyassu F; Shirley R; Hu CH; Dare AJ; James AM; Rogatti S; Hartley RC; Eaton S; Costa ASH; Brookes PS; Davidson SM; Duchen MR; Saeb-Parsy K; Shattock MJ; Robinson AJ; Work LM; Frezza C; Krieg T; Murphy MP Ischaemic accumulation of succinate controls reperfusion injury through mitochondrial ROS. Nature 2014, 515, 431–435. [PubMed: 25383517]

(9). Zhai Y; Petrowsky H; Hong JC; Busuttil RW; Kupiec-Weglinski JW Ischaemia-reperfusion injury in liver transplantation–from bench to bedside. Nat. Rev. Gastroenterol. Hepatol 2013, 10, 79–89. [PubMed: 23229329]

(10). Rajkovic O; Gourmel C; d'Arcy R; Wong R; Rajkovic I; Tirelli N; Pinteaux EJAT Reactive Oxygen Species-Responsive Nanoparticles for the Treatment of Ischemic Stroke. Adv. Ther 2019, 2, 1900038.

(11). Kwon HJ; Cha MY; Kim D; Kim DK; Soh M; Shin K; Hyeon T; Mook-Jung I Mitochondria-Targeting Ceria Nanoparticles as Antioxidants for Alzheimer's Disease. ACS Nano 2016, 10, 2860–70. [PubMed: 26844592]

(12). Ni D; Jiang D; Kutyreff CJ; Lai J; Yan Y; Barnhart TE; Yu B; Im H-J; Kang L; Cho SY; Liu Z; Huang P; Engle JW; Cai W Molybdenum-based nanoclusters act as antioxidants and ameliorate acute kidney injury in mice. Nat. Commun 2018, 9, 1–11. [PubMed: 29317637]

(13). Wang Y; Li L; Zhao W; Dou Y; An H; Tao H; Xu X; Jia Y; Lu S; Zhang J; Hu H Targeted Therapy of Atherosclerosis by a Broad-Spectrum Reactive Oxygen Species Scavenging Nanoparticle with Intrinsic Anti-inflammatory Activity. ACS Nano 2018, 12, 8943–8960. [PubMed: 30114351]

(14). Dkhil M; Zrieq R; Al-Quraishy S; Abdel Moneim A Selenium nanoparticles attenuate oxidative stress and testicular damage in streptozotocin-induced diabetic rats. Molecules 2016, 21, 1517.

(15). Pedone D; Moglianetti M; De Luca E; Bardi G; Pompa PP Platinum nanoparticles in nanobiomedicine. Chem. Soc. Rev 2017, 46, 4951–4975. [PubMed: 28696452]

(16). Somasuntharam I; Yehl K; Carroll SL; Maxwell JT; Martinez MD; Che P-L; Brown ME; Salaita K; Davis ME Knockdown of TNF-α by DNAzyme gold nanoparticles as an anti-inflammatory therapy for myocardial infarction. Biomaterials 2016, 83, 12–22. [PubMed: 26773660]

(17). Bhattacharjee A; Basu A; Sen T; Biswas J; Bhattacharya S Nano-Se as a novel candidate in the management of oxidative stress related disorders and cancer. Nucleus 2017, 60, 137–145.

(18). Chen J; Patil S; Seal S; McGinnis JF Rare earth nanoparticles prevent retinal degeneration induced by intracellular peroxides. Nat. Nanotechnol 2006, 1, 142. [PubMed: 18654167]

(19). Asati A; Santra S; Kaittanis C; Nath S; Perez JM Oxidase-like activity of polymer-coated cerium oxide nanoparticles. Angew. Chem., Int. Ed 2009, 48, 2308–2312.

(20). Lu D; Zhou J; Hou S; Xiong Q; Chen Y; Pu K; Ren J; Duan HJAM Functional Macromolecule-Enabled Colloidal Synthesis: From Nanoparticle Engineering to Multifunctionality. Adv. Mater 2019, 31, 1902733.

(21). Wang D; Lin Z; Wang T; Yao Z; Qin M; Zheng S; Lu WJJ o. h. m. Where does the toxicity of metal oxide nanoparticles come from: the nanoparticles, the ions, or a combination of both? J. Hazard. Mater 2016, 308, 328–334. [PubMed: 26852208]

(22). Dugan LL; Turetsky DM; Du C; Lobner D; Wheeler M; Almli CR; Shen CK-F; Luh T-Y; Choi DW; Lin T-S Carboxyfullerenes as neuroprotective agents. Proc. Natl. Acad. Sci. U. S. A 1997, 94, 9434–9439. [PubMed: 9256500]

(23). Quick KL; Ali SS; Arch R; Xiong C; Wozniak D; Dugan LL A carboxyfullerene SOD mimetic improves cognition and extends the lifespan of mice. Neurobiol. Aging 2008, 29, 117–128. [PubMed: 17079053]

(24). Gharbi N; Pressac M; Hadchouel M; Szwarc H; Wilson SR; Moussa F [60] Fullerene is a powerful antioxidant in vivo with no acute or subacute toxicity. Nano Lett. 2005, 5, 2578–2585. [PubMed: 16351219]

(25). Baccile N; Laurent G; Babonneau F; Fayon F; Titirici M-M; Antonietti M Structural characterization of hydrothermal carbon spheres by advanced solid-state MAS 13C NMR investigations. J. Phys. Chem. C 2009, 113, 9644–9654.

(26). Lucente-Schultz RM; Moore VC; Leonard AD; Price BK; Kosynkin DV; Lu M; Partha R; Conyers JL; Tour JM Antioxidant single-walled carbon nanotubes. J. Am. Chem. Soc 2009, 131, 3934–3941. [PubMed: 19243186]

(27). Qiu Y; Wang Z; Owens AC; Kulaots I; Chen Y; Kane AB; Hurt RH Antioxidant chemistry of graphene-based materials and its role in oxidation protection technology. Nanoscale 2014, 6, 11744–11755. [PubMed: 25157875]

(28). Sun X; Li Y Colloidal carbon spheres and their core/shell structures with noble-metal nanoparticles. Angew. Chem., Int. Ed 2004, 43 (5), 597–601.

(29). Fukuhara K; Nakajima K; Kitano M; Kato H; Hayashi S; Hara M Structure and catalysis of cellulose-derived amorphous carbon bearing SO3H groups. ChemSusChem 2011, 4, 778–784. [PubMed: 21595046]

(30). Zheng M; Liu Y; Jiang K; Xiao Y; Yuan D Alcohol-assisted hydrothermal carbonization to fabricate spheroidal carbons with a tunable shape and aspect ratio. Carbon 2010, 48, 1224–1233.

(31). Ferrari AC; Robertson J Interpretation of Raman spectra of disordered and amorphous carbon. Phys. Rev. B: Condens. Matter Mater. Phys 2000, 61, 14095.

(32). Schwan J; Ulrich S; Batori V; Ehrhardt H; Silva S Raman spectroscopy on amorphous carbon films. J. Appl. Phys 1996, 80, 440–447.

(33). Zhang Y; Hong H; Cai W PET tracers based on Zirconium-89. Curr. Radiopharm 2011, 4, 131–139. [PubMed: 22191652]

(34). Dobrovolskaia MA; Aggarwal P; Hall JB; McNeil SE Preclinical studies to understand nanoparticle interaction with the immune system and its potential effects on nanoparticle biodistribution. Mol. Pharmaceutics 2008, 5, 487–495.

(35). Chen F; Goel S; Valdovinos HF; Luo H; Hernandez R; Barnhart TE; Cai W In vivo integrity and biological fate of chelator-free zirconium-89-labeled mesoporous silica nanoparticles. ACS Nano 2015, 9, 7950–7959. [PubMed: 26213260]

(36). Tsung A; Sahai R; Tanaka H; Nakao A; Fink MP; Lotze MT; Yang H; Li J; Tracey KJ; Geller DA; Billiar TR The nuclear factor HMGB1 mediates hepatic injury after murine liver ischemia-reperfusion. J. Exp. Med 2005, 201, 1135–43. [PubMed: 15795240]

(37). Suzuki S; Toledo-Pereyra L; Rodriguez F; Cejalvo DJT Neutrophil infiltration as an important factor in liver ischemia and reperfusion injury. Modulating effects of FK506 and cyclosporine. Transplantation 1993, 55, 1265–1271. [PubMed: 7685932]

(38). Amacher DE Serum transaminase elevations as indicators of hepatic injury following the administration of drugs. Regul. Toxicol. Pharmacol 1998, 27, 119–130. [PubMed: 9671567]

(39). Nishimura T; Yoshida Y; Watanabe F; Koseki M; Nishida T; Tagawa K; Kawashima Y Blood level of mitochondrial aspartate aminotransferase as an indicator of the extent of ischemic necrosis of the rat liver. Hepatology 1986, 6, 701–707. [PubMed: 2426171]

(40). Landis GN; Tower J Superoxide dismutase evolution and life span regulation. Mech. Ageing Dev 2005, 126, 365–379. [PubMed: 15664623]

(41). Zhang W; Wang M; Xie H; Zhou L; Meng X; Shi J; Zheng S Role of reactive oxygen species in mediating hepatic ischemia-reperfusion injury and its therapeutic applications in liver transplantation In Transplantation Proceedings; Elsevier, 2007; pp 1332–1337.

(42). Bilzer M; Roggel F; Gerbes AL Role of Kupffer cells in host defense and liver disease. Liver Int. 2006, 26, 1175–86. [PubMed: 17105582]

(43). Muto Y; Meager A; Nouri-Aria K; Alexander GM; Eddleston AW; Williams RJ Enhanced tumour necrosis factor and interleukin-1 in fulminant hepatic failure. Lancet 1988, 332, 72–74.

(44). Feldstein AE; Werneburg NW; Canbay A; Guicciardi ME; Bronk SF; Rydzewski R; Burgart LJ; Gores GJ Free fatty acids promote hepatic lipotoxicity by stimulating TNF-α expression via a lysosomal pathway. Hepatology 2004, 40, 185–194. [PubMed: 15239102]

(45). Coleman JW Nitric oxide in immunity and inflammation. Int. Immunopharmacol 2001, 1, 1397–1406. [PubMed: 11515807]

(46). Kolaczkowska E; Kubes P Neutrophil recruitment and function in health and inflammation. Nat. Rev. Immunol 2013, 13, 159–75. [PubMed: 23435331]

(47). Murray PJ; Wynn TA Protective and pathogenic functions of macrophage subsets. Nat. Rev. Immunol 2011, 11, 723. [PubMed: 21997792]

(48). Perry BC; Soltys D; Toledo AH; Toledo-Pereyra LH Tumor Necrosis Factor-α in Liver Ischemia/Reperfusion Injury. J. Invest. Surg 2011, 24, 178–188. [PubMed: 21675854]

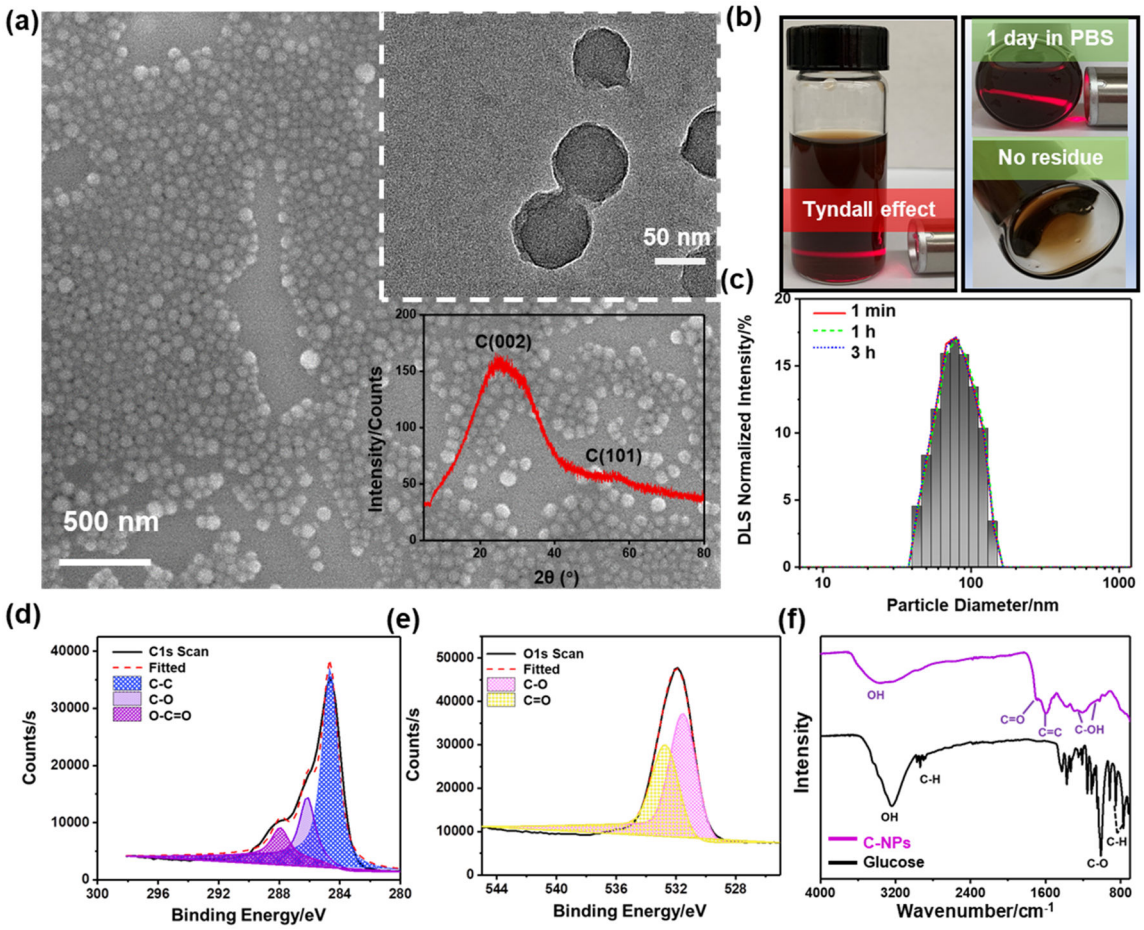

Figure 1.

Physiochemical characterization of C-NPs. (a) SEM and TEM (top-inset) images and XRD spectra (bottom-inset) of as-prepared C-NPs. (b) Photograph of C-NPs dispersed in PBS solution. (c) DLS size distribution of C-NPs in water at different time point. (d,e) XPS C 1s and O 1s spectra of C-NPs, respectively. (f) FTIR spectra of C-NPs and the parent carbohydrate glucose.

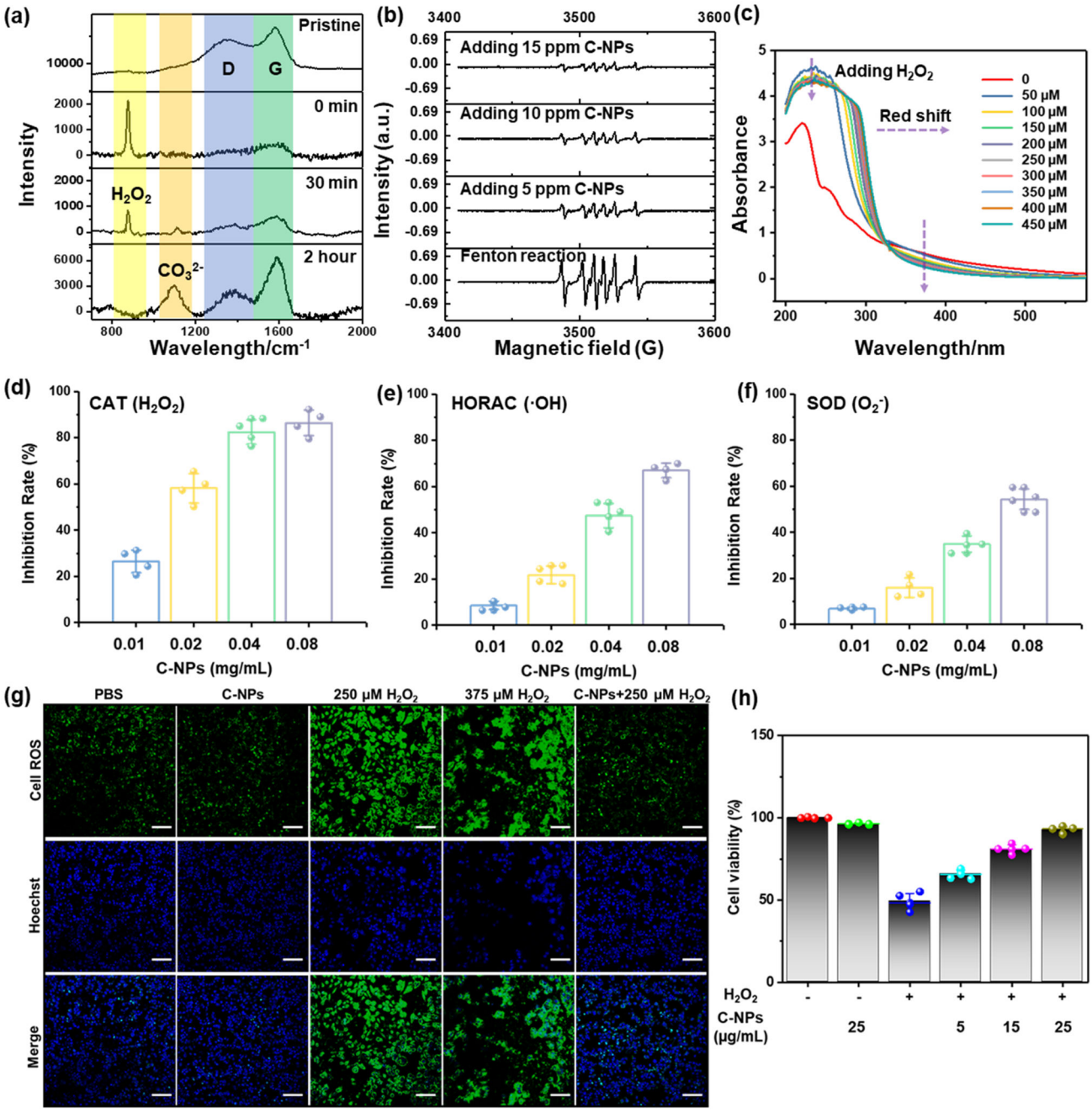

Figure 2.

In vitro ROS scavenging capability of C-NPs. (a) *In situ* Raman spectra of C-NPs reacting with H_2O_2 at varied time points (0, 30 min, and 2 h). (b) ESR spectra of different groups using DMPO as spin trap agent. (c) UV–vis spectra of C-NPs reacting with varied concentrations of H_2O_2. (d–f) ROS scavenging activity of C-NPs to CAT (d), HORC (e), and SOD (f). Data represent mean ± s.d. from four independent replicates. (g) Immunofluorescent staining image of HepG2 cells incubated in different environments by using CellROX for ROS staining (Green) (top row) and Hoechst for nuclei staining (blue) (middle row) and merged image (bottom row). Scale bar: 100 μm. (h). *In vitro* cell viabilities

of HEK293 cells with(+)/without(−) H_2O_2 and adding different concentrations of C-NPs (5–25 μg/mL).

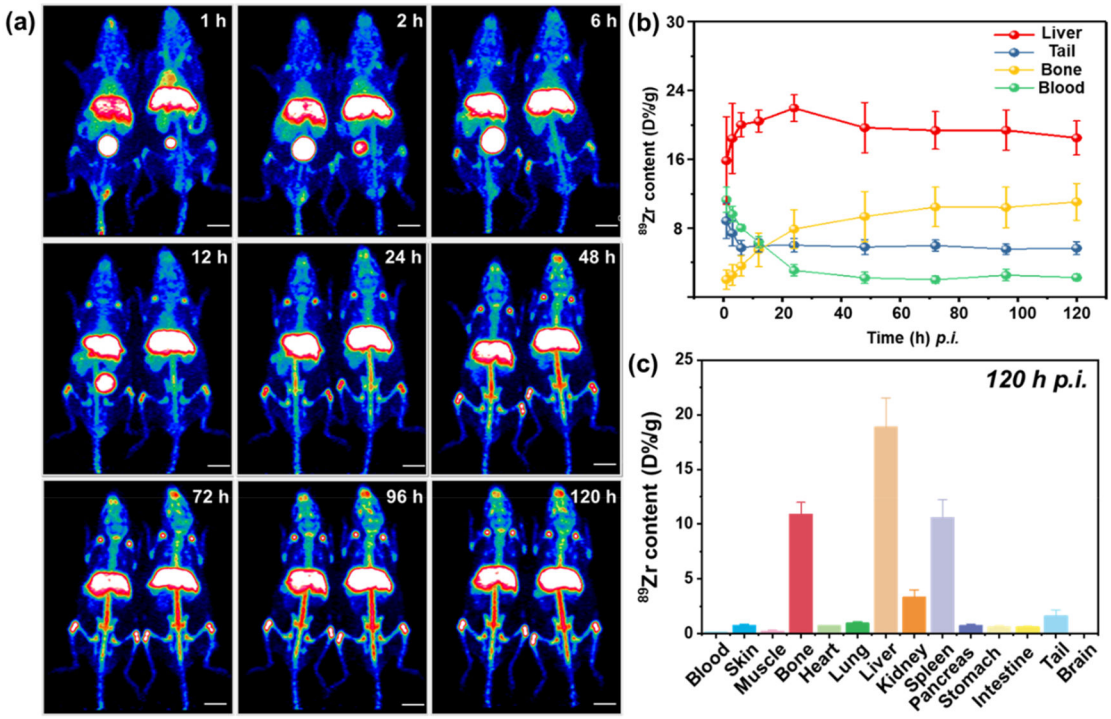

Figure 3.

In vivo PET imaging and quantification in organs. (a) Representative maximum intensity projection (MIP) of PET images after i.v. injection of ^{89}Zr–C–NPs at different time points. (b) Quantification of time-activity curve of ^{89}Zr–C–NPs in the liver, tail, bone, and blood at various time points p.i. (c) Quantification of ^{89}Zr–C–NPs in major body areas after 120 h p.i.

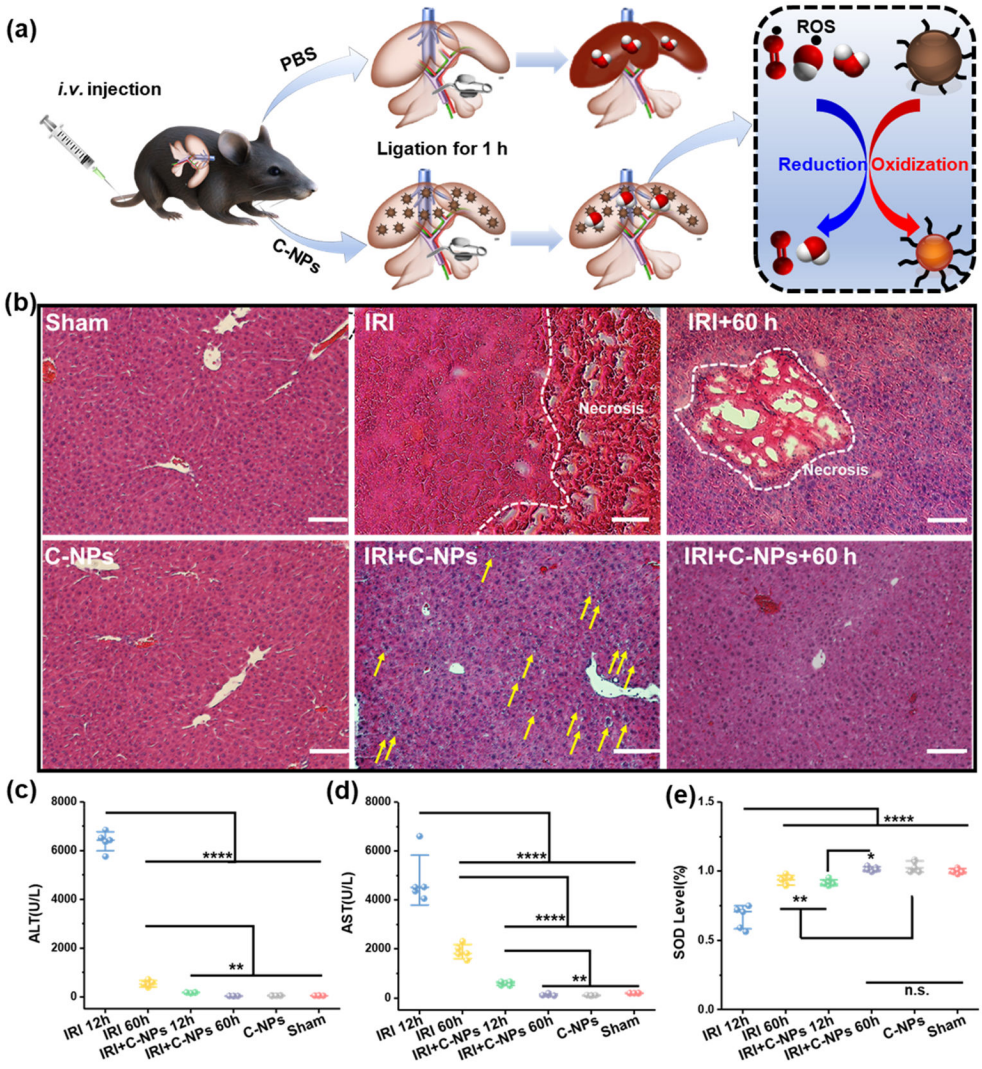

Figure 4.

Hepatic IRI prevention performance of C-NPs in mice model. (a) Schematic of the Hepatic IRI generation and treatment. (b) H&E staining of liver tissues from each group. Yellow arrows indicate slight vacuolization, and the white dashed lines show the severe cytolysis, nucleus dissolving, and necrosis of the liver cells. Scale bar: 100 μm. (c) ALT, (d) AST, and (e) SOD levels in liver homogenates from each group. Data represent mean ± s.d. from five independent replicates, and *P* values were calculated by one-way ANOVA with Tukey's honest significant difference posthoc test (**** $p < 0.0001$).

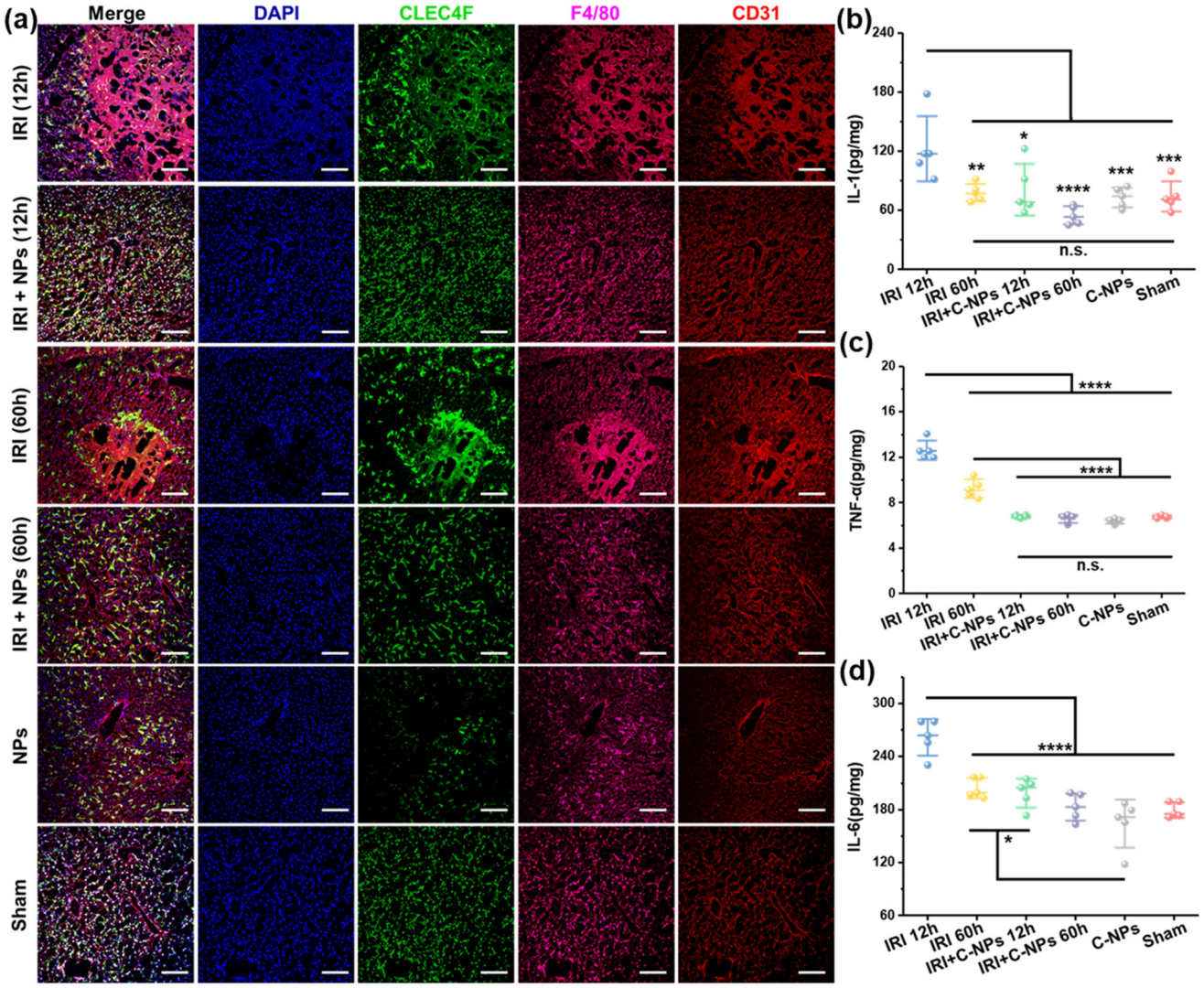

Figure 5.

Immunofluorescence staining and dection of cytokines of liver samples. (a) Immunofluorescence staining of liver samples by using DAPI (blue) for nuclear stainging, anti-CLE4F antibody (green) as Kupffer cell marker, anti-F4/80 antibody (pink) as monocyte/macrophage marker, and anti-CD31 antibody (red) as an endothelial marker in liver homogenates from each group. Scale bar: 100 μm. Cytokines of IL-1 (b), TNF-α (c), and IL-6 (d) from activated monocyte/macrophages and Kupffer cells were measured in liver homogenates from each group by ELISA. Data represent mean ± s.d. from five independent replicates, and *P* values were calculated by one-way ANOVA with Tukey's honest significant difference posthoc (* $p < 0.05$; ** $p < 0.01$; *** $p < 0.001$; **** $p < 0.0001$)